Astronomy & Astrophysics manuscript no. aanda
March 24, 2023

The Brighter-Fatter Effect in the JWST MIRI Si:As IBC detectors

I. Observations, impact on science, and modelling

Ioannis Argyriou[1], Craig Lage[2], George H. Rieke[3], Danny Gasman[1], Jeroen Bouwman[4], Jane Morrison[3], Mattia Libralato[5], Daniel Dicken[6], Bernhard R. Brandl[7,8], Javier Álvarez-Márquez[9], Alvaro Labiano[9,10], Michael Regan[11], and Michael E. Ressler[12]

[1] Institute of Astronomy, KU Leuven, Celestijnenlaan 200D, 3001 Leuven, Belgium
[2] Department of Physics, University of California-Davis, 1 Shields Ave. Davis, Ca., U.S.A.
[3] Steward Observatory and the Department of Astronomy, The University of Arizona, 933 N Cherry Ave, Tucson, AZ, 85750, USA
[4] Max Planck Institute for Astronomy, Königstuhl 17, D-69117 Heidelberg, Germany
[5] AURA for the European Space Agency (ESA), Space Telescope Science Institute, 3700 San Martin Drive, Baltimore, MD 21218, USA
[6] UK Astronomy Technology Centre, Royal Observatory Edinburgh, Blackford Hill, Edinburgh EH9 3HJ, UK
[7] Leiden Observatory, Leiden University, PO Box 9513, 2300 RA Leiden, The Netherlands
[8] Faculty of Aerospace Engineering, Delft University of Technology, Kluyverweg 1, 2629 HS Delft, The Netherlands
[9] Telespazio UK for the European Space Agency, ESAC, Camino Bajo del Castillo s/n, 28692 Villanueva de la Cañada, Spain.
[10] Centro de Astrobiología (CAB), CSIC-INTA, ESAC, Carretera de Ajalvir km4, 28850 Torrejón de Ardoz, Madrid, Spain.
[11] Space Telescope Science Institute, 3700 San Martin Drive, Baltimore, MD, 21218, USA
[12] Jet Propulsion Laboratory, California Institute of Technology, 4800 Oak Grove Dr., Pasadena, CA, 91109, USA
e-mail: ioannis.argyriou@kuleuven.be

Received March 24, 2023

ABSTRACT

Context. The Mid-Infrared Instrument (MIRI) on board the James Webb Space Telescope (*JWST*) uses three Si:As impurity band conduction (IBC) detector arrays. The output voltage level of each MIRI detector pixel is digitally recorded by sampling-up-the-ramp. For uniform or low-contrast illumination, the pixel ramps become non-linear in a predictable way, but in areas of high contrast, the non-linearity curve becomes much more complex.

Aims. We provide observational evidence of the Brighter-Fatter Effect (BFE) in MIRI conventional and high-contrast coronographic imaging, low-resolution spectroscopy, and medium-resolution spectroscopy data and investigate the physical mechanism that gives rise to the effect on the detector pixel raw voltage integration ramps.

Methods. We use public data from the *JWST*/MIRI commissioning and Cycle 1 phase. We also develop a numerical electrostatic model of the MIRI detectors using a modified version of the public Poisson_CCD code.

Results. The physical mechanism behind the MIRI BFE is fundamentally different to that of CCDs and Hawaii-2RG (H2RG) detectors. This is due to the largest majority of the MIRI photo-excited electric charges not being stored at the pixels but at the input to the MIRI detector unit cell buffer amplifier capacitance. The resulting detector voltage debiasing alters the electrostatic potential inside the infrared-active layer and causes new photo-excited electrons, generated at a bright pixel, to be guided to the neighboring fainter pixels. Observationally, the debiasing-induced BFE makes the *JWST* MIRI data yield 10 – 25 % larger and 0.5 – 8 % brighter point sources and spectral line profiles as a function of the output level covered by the detector pixels. We find that the profile of the shrinking detector depletion region has implications for developing a pixel ramp non-linearity model for point sources observed with MIRI.

Key words. Astronomical instrumentation, methods and techniques – Instrumentation: detectors – Methods: data analysis – Methods: numerical – Infrared: general

1. Introduction

The Mid-Infrared Instrument MIRI (Wright, et al. 2023), on board the *James Webb Space Telescope (JWST)*, has four observing modes, (1) imaging, (2) low-resolution spectroscopy, (3) high-contrast (coronagraphic) imaging, and (4) medium-resolution spectroscopy (Wright et al. 2015; Bouchet et al. 2015; Kendrew et al. 2015; Boccaletti et al. 2015; Wells et al. 2015). In total MIRI uses three Si:As impurity band conduction (IBC) detector arrays, one for conventional imaging, high-contrast imaging and low-resolution spectroscopy, and two for medium-resolution spectroscopy (Rieke et al. 2015). Si:As IBC devices have extensive space flight heritage, having been used for example in all three instruments of the Spitzer space telescope, namely the Infrared Array Camera (IRAC), the Infrared Spectrograph (IRS), and the Multiband Imaging Photometer (MIPS). The high quantum efficiency of the Si:As IBC devices, in combination with the extensive wavelength range covered (5-28 μm) gives these devices a unique advantage (Love et al. 2005; Gáspár et al. 2021). Other detectors, such as the Teledyne Imaging Sensors' LWIR HgCdTe detector have a relatively higher quantum effi-

ciency, however, they cover a shorter wavelength range, namely out to 13 μm[1] (Dorn et al. 2018).

The Brighter-Fatter Effect (BFE) is a well-known detector effect that blurs the intrinsic spatial and spectral information of a source. For Charge-Coupled Devices (CCDs) and Hawaii-2RG (H2RG) detectors, operating in the optical and near-infrared, the effect has been shown to manifest due to the build-up of a transverse electric field at the pixel surface following the accumulation of photo-excited electrons at the pixel surface (Lage et al. 2017; Coulton et al. 2018; Plazas et al. 2018; Hirata & Choi 2020). Further accumulation of photo-excited electrons is hindered by the transverse electric field that results in the electron paths curving to neighboring pixels. Both the *JWST* NIRCam and NIRSpec instruments use H2RG detectors and show this effect. The BFE has been found to also impact MIRI data. However, due to the low capacitance at the MIRI detector pixels, the physical mechanism causing the MIRI BFE is difficult to fit within the traditional CCD and H2RG picture.

In this paper we describe the many facets of the BFE systematic effect on the MIRI detector pixel output signal across all the MIRI observing modes, the impact this effect has on the science, as well as develop a model that explains the physical mechanism of the effect for the Si:As IBC detectors. In Sect. 2 we describe how the MIRI detector arrays work, how they produce the raw output signal used to estimate the flux from astronomical sources, and how the detector pixel non-linear behavior to non-uniform illumination affects the raw output signal. In Sect. 3 we show and describe how the MIRI BFE impacts the scientific interpretation of MIRI imaging, low-resolution spectroscopy, medium-resolution spectroscopy and high contrast (coronographic) imaging. In Sect. 4 we present a realistic electrostatic model of the MIRI detectors, that illustrates the physical mechanism behind the effect, using the public `Poisson_CCD` numerical code (Lage et al. 2021). We also present the results of the electrostatic simulations, limiting the simulations to the imaging case. In Sect. 5 the implications of the presented results are discussed, and the conclusions of this study are formulated in Sect. 6.

2. The *JWST* MIRI detectors and the pixel non-linear response to non-uniform illumination

2.1. The detector architecture

To understand the MIRI BFE, an in-depth understanding of the Si:As IBC detector architecture and read-out integration circuit (ROIC) is required. We describe these first, starting from a representation of the architecture of the MIRI detector arrays, shown in Fig. 1. Si:As IBC detectors are grown on a silicon substrate. Photons pass through the anti-reflection coating on the detector back side, into the substrate, and then through the ion-implanted buried contact into the infrared-active layer (detection layer). The infrared-active layer is doped with arsenic to absorb the incoming photons, which elevate photo-excited electrons from the impurity band into the conduction band. Assuming a low level of minority acceptor impurities in this layer, an electric field can be maintained across it that causes the photo-excited electrons to migrate to the front of the detector. A thin, high purity layer (blocking layer) is grown over the front of the infrared-active layer. When operated at sufficiently low temperatures, thermally-generated free charge carriers cannot penetrate the blocking layer because it lacks an impurity band and the carriers have insufficient energy to be lifted into the conduction band (a band diagram for front-illuminated Si:As IBC detectors can be found in Rieke (2003)). The photo-generated free charge carriers in the conduction band can, however, traverse the blocking layer, to be collected at the front contact. The electric field that drives this process is maintained across the infrared-active layer between the front contact, on the readout side, and the buried contact, connected via a V-etch buried implant. The photo-excited electrons are transferred through an ion-implanted transition region to a metalized output pad. The indium bump conveys the signal to a matching input pad on a readout amplifier. The MIRI detector operational temperature of 6.4 K keeps the detector dark current very low (< 0.1 e$^-$/s) (Rieke et al. 2015).

The MIRI detector bias voltage V_{bias} is defined by Eq. 1 (Ressler et al. 2015).

$$V_{bias} = V_{dduc} - V_{detcom} + 0.2V, \quad (1)$$

where V_{dduc} is the voltage of the front contact, and V_{detcom} is the voltage of the buried contact. The bias voltage is set whenever the reset switch is closed. After the reset switch is opened, the signal from a detector pixel is accumulated as a reduction in the voltage from V_{bias}. The voltage from the detector is buffered by an analog Field Effect Transistor (FET) within the pixel unit cell.

The signal is passed to the output by operating the row and column switches (a single row is shown in Fig. 1). Shown at the bottom of Fig. 1 are the five MIRI detector video lines, each with its own read-out amplifier. Amplifiers 1 to 4 (video lines 1 to 4) address the first to fourth pixel columns from left to right, respectively. In the case of permanent loss of one of these four video lines, this would result in the loss of an alternating fourth column of array imagery. Amplifier 5 (video reference line), which is not shown in Fig. 1, addresses a group of "blind" pixels. These are not physical pixels; the amplifier is connected to a reference impedance similar to the resistance of a detector pixel. The purpose of this reference line is to provide a reference output that can be used for engineering and data quality-monitoring purposes; however, we believe a design flaw limits the utility of this output in actuality.

2.2. The MIRI detector pixel read-out

The MIRI focal plane module (FPM) focal plane electronics (FPE) measure signal in the form of integration ramps. These form the MIRI raw data that will be discussed throughout this paper. MIRI pixels are read non-destructively (charge is read but not reset). An illustration of an ideal pixel integration ramp is shown in Fig. 2. On the x-axis is the image frame number, and on the y-axis is the output level of a video line. The read-out electronics represent the voltage difference as accumulated Digital Numbers (DN). The proportionality between the accumulated DN and the voltage difference is defined by the system gain.

Whenever the detectors are idle (non-exposing) the pixels are constantly resetting at the frame rate. In this case the amplifier integrating node voltage remains close to the bias voltage. An exposure starts when the reset switch is opened, as shown in Fig. 1. At that point, with the reset switch kept open, the amplifier integration node voltage changes based on the photoelectric current. The current depends on the number of photons detected. The time difference between two pixels being read out is set by the FPE master 100 kHz clock ($t_d = 10\ \mu s$) (Ressler et al. 2015). After the first pixel is read out (pixel (1,1) in Fig. 2), all

[1] The Teledyne Imaging Sensors' LWIR HgCdTe detectors were not available at the time of the detector selection for MIRI.

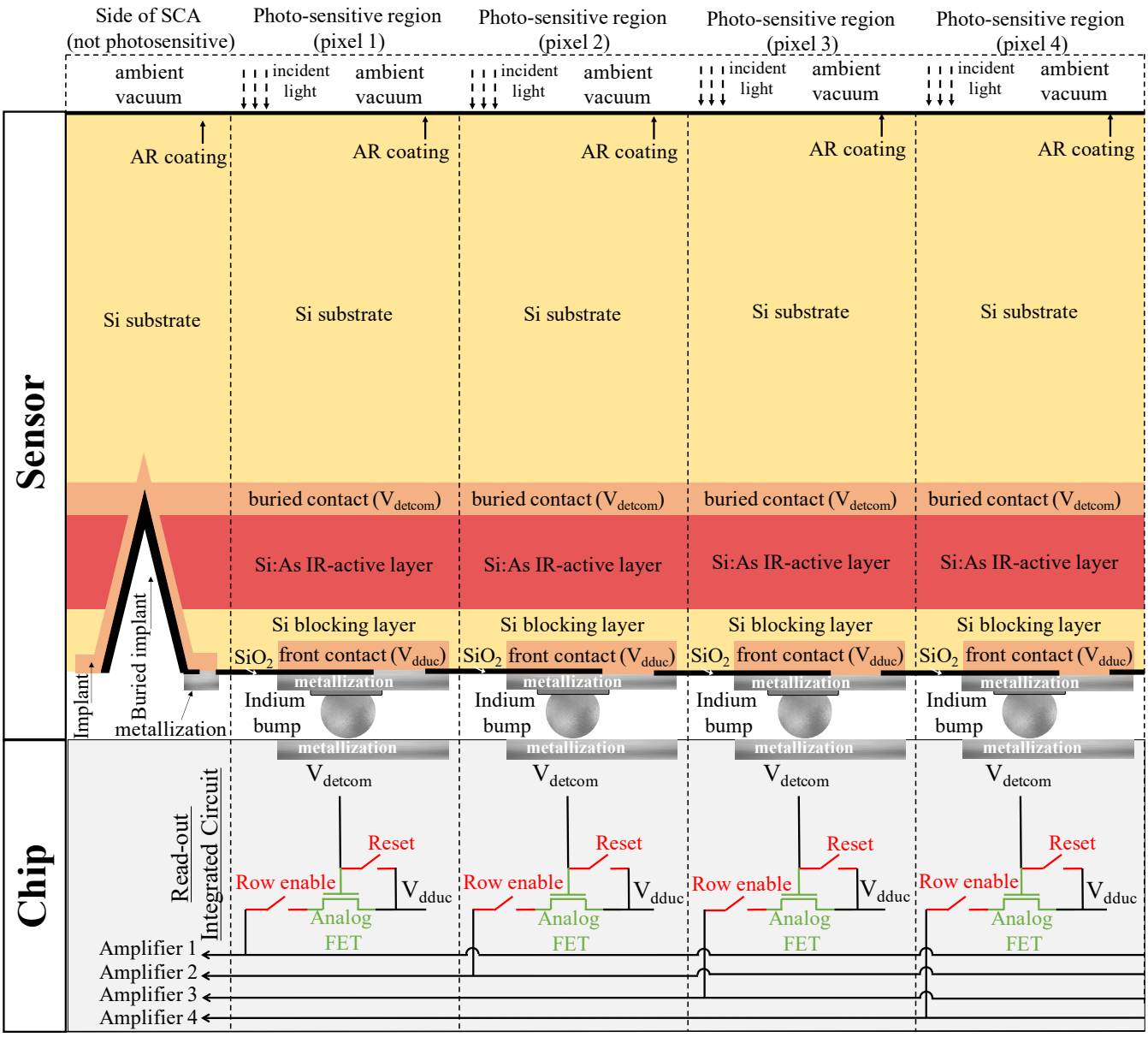

Fig. 1. Representation of MIRI detector architecture based on Petroff & Stapelbroek (1986); Love et al. (2005); Rieke et al. (2015); Gáspár et al. (2021)]. The dimensions are not to scale.

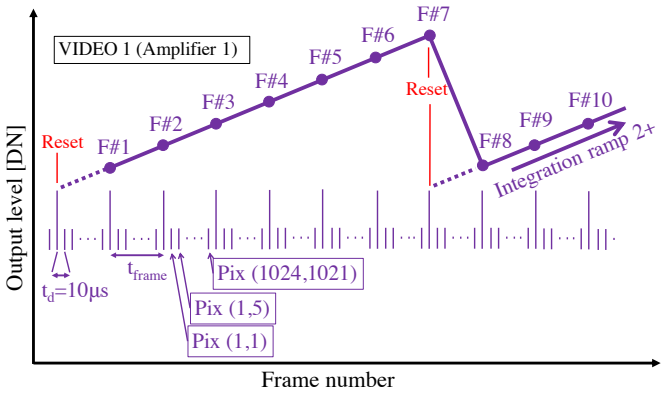

Fig. 2. Conceptual representation of a MIRI detector pixel integration ramp. Individual frames are designated by F#.

other pixels on the detector have to be read out before the first pixel can be read out again. The five amplifiers are read out at the same time. Specifically, taking row 1 as an example, pixels (1,5,9,...,1021) addressed by Amplifier 1, are read at the same time as pixels (2,6,10,...,1022) addressed by Amplifier 2, and so on. Every time the detector is read out in its entirety, a detector frame is stored (equivalent to one frame number in Fig. 2). At the end of an integration, the reset switch is closed and the node voltage returns to the bias voltage. MIRI observers can take multiple integrations in a single exposure, and in that case, after a virtually instantaneous reset, the pixel starts integrating signal again. The default operation of the MIRI FPE in flight is to perform two reset frames in succession to mitigate reset switch charge decay effects, i.e., once to remove the integrated signal and again to set a solid zero point (Morrison, et al. 2023).

A 16-bit register such as the one used by the MIRI FPE can store up to 2^{16} different values, i.e. 65536 different values going from 0 DN up to 65535 DN. The MIRI detector output is

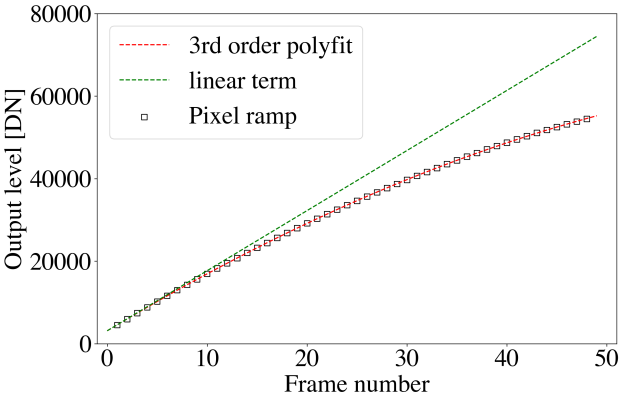

Fig. 3. Non-linearity in MIRI pixel ramp (black squares). A second order polynomial is fitted to the ramp (red dashed line). The dashed green line shows the linear term of the second order fit.

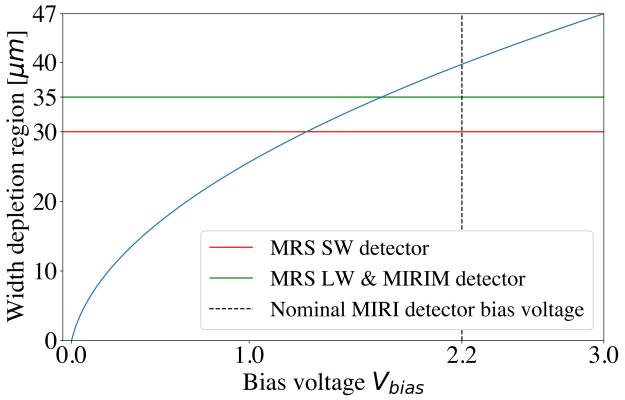

Fig. 4. Width of MIRI detector depletion region as a function of bias voltage. The nominal MIRI detector bias voltage is 2.2 V for all three MIRI detectors (Ressler et al. 2015).

approximately +0.5 Volt for zero signal and -1.0 Volt for saturation. Ideally, the detector +0.5 V would be read as 0 DN, and -1.0 V would be read as 65535 DN, however, this is not the case. The detector range is not mapped to the full analog-to-digital converter range. Ressler et al. (2015), estimated a net system gain of the MIRI detectors of 38300 DN/V, so +0.5 V to -1.0 V changes only 57450 DN. Rieke et al. (2015), report that "the detector is a simple plane-parallel 1.1 fF capacitor, the indium bump bonds may contribute an additional ~4 fF to the node capacitance (Moore, Andrew C. 2005), and the capacitance at the input to the [pixel] unit cell buffer amplifier is 28.5 fF (McMurtry et al. 2005), thus the nominal capacitance at the integrating node is 33.6 fF". Using these capacitance values and the net system gain, Rieke et al. (2015) derived a pixel gain of 5.5 e^-/DN. However, this value was uncertain due to a number of effects, particularly interpixel capacitance. Experience in flight has indicated a smaller pixel gain value, but this is still work in progress.

2.3. The non-linearity of the MIRI detector pixel voltage integration ramps

Similar to most other detectors used in astronomical observing applications, the MIRI detector pixel integration ramps suffer from a non-linear response as a function of the DN output level. An example of a MIRI pixel ramp is shown in Fig. 3. Instead of the output level increasing linearly with frame number (time) the slope of the ramp decreases. Traditionally a correction for this non-linearity is derived by (1) fitting a polynomial to the ramp, (2) using the linear term of the fit as a proxy for what the ramp would look like if not impacted by the cause behind the non-linearity, (3) a correction is defined as the ratio of the linear term and the polynomial fit, and that as a function of the DN level at each frame time (Morrison, et al. 2023).

On a system level, for the MIRI Si:As IBC detectors, non-linearity is caused by a reduction in detector responsivity with increasing charge accumulation at the amplifier integrating node capacitance (Rieke et al. 2015). A voltage $V_{dduc} = -2.0$ V is applied at the front contact and a voltage $V_{detcom} = -4.0$ V is applied at the detector buried contact. An additional 0.2 V is applied on the amplifier node capacitance, for a total detector bias voltage $V_{bias} = 2.2$ V, as formulated in Eq. 1. Under these conditions the region between the front contact and the buried contact becomes fully depleted of free charge carriers. Photoelectrons are produced throughout the depletion region (infrared-active layer) and the electric field causes them to migrate towards the pixels. The MIRI detector bias voltage of 2.2 V was tuned for the width of the depletion region to cover the entire active layer without causing avalanche gain (Rieke et al. 2015). However, charge accumulation at the amplifier integrating node capacitance reduces the net bias voltage on the detector. As a result, at higher DN levels the net bias voltage decreases, the width of the depletion region shrinks below the active layer width, and a smaller fraction of the produced photoelectrons are guided to the pixels, resulting in a reduction in detector responsivity as a function of DN.

The 1D equation for the width of the MIRI detector depletion region is mathematically described by Eq. 2 (Pierret & Harutunian 1996; Rieke et al. 2015).

$$w = \left[\frac{2\kappa_0\varepsilon_0}{qN_A}\,|V_{bias}| + t_B^2\right]^{1/2} - t_B, \tag{2}$$

here w is the width of the depletion region, $\kappa_0 = 11.68$ is the dielectric constant of silicon, $\varepsilon_0 = 8.854 * 10^{-12}\ \frac{C}{V*m}$ is the permittivity of free space, $q = 1.6 * 10^{-19}$ C is the elementary charge, $N_A = 1.5 * 10^{12}$ cm^{-3} is the density of the minority (acceptor) impurity concentration in the MIRI detector active layer, $V_{bias} = 2.2$ V is the bias voltage, and $t_B = 4\ \mu m$ is the width of the detector blocking layer (Love et al. 2005; Rieke et al. 2015). We use these values to plot the width of the depletion region w as a function of bias voltage V_{bias} in Fig. 4. Based on the provided values we find that for a bias voltage V_{bias}=2.2 V the depletion region covers the full MRS short wavelength (SW), long wavelength (LW) detectors, and imaging (MIRIM) detector.

For an accumulated DN value of 50000 DN, if we use the net system gain value of 38300 DN/V of Rieke et al. (2015), we estimate a debiasing of ~1.3 V. Tracing this back to Fig. 4, at that level of debiasing the width of the depletion region is much less than the active layer width of both the MRS SW detector, LW detector, and MIRIM detector. Photo-excited electrons in the undepleted region can still be collected if they diffuse to the depleted region, but at reduced efficiency. This is the cause of the non-linearity at higher accumulated DN shown in Fig. 3. Calibrating the non-linearity effect due to the detector debiasing is equivalent to predicting what the output DN level would be if the active layer was always fully depleted.

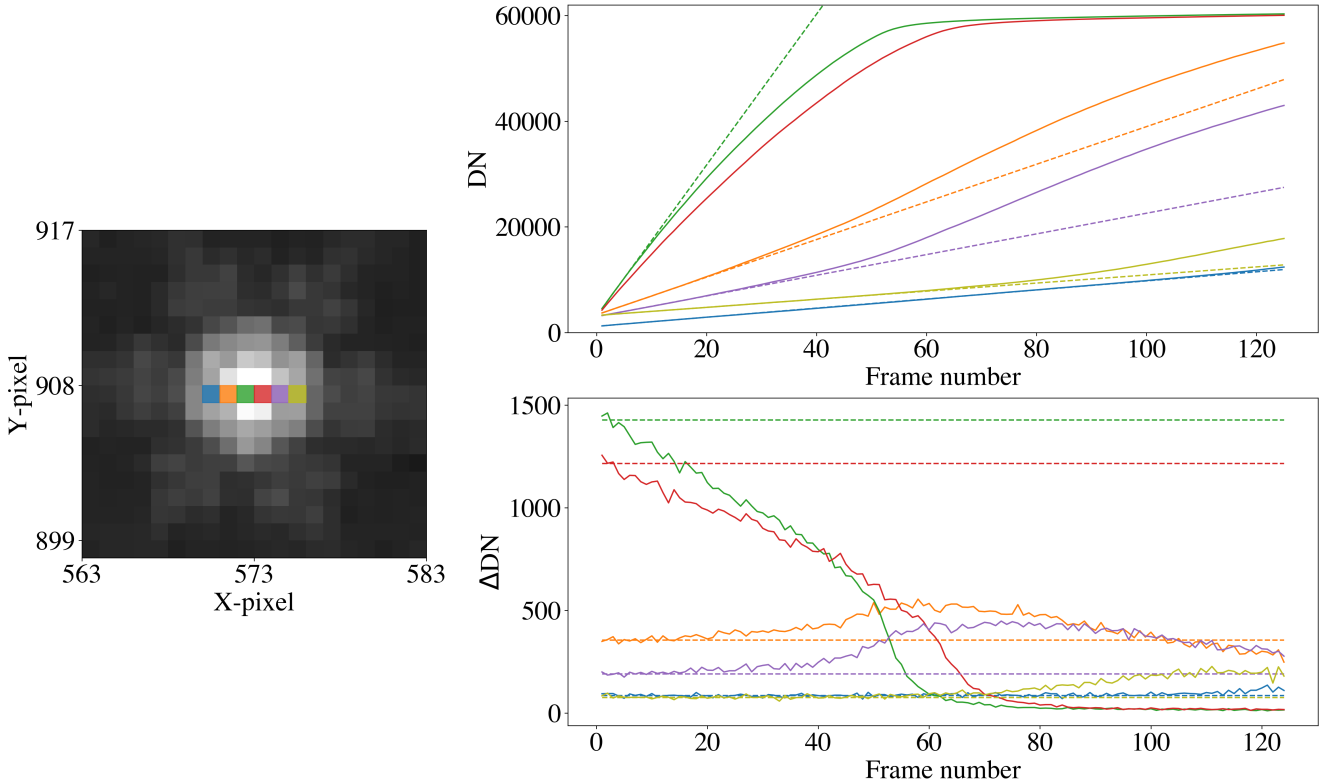

Fig. 5. Left: Reduced MIRI imaging data of an unresolved (point) source taken with the F560W filter (plotted in log scale). Six pixels are selected across the horizontal width of the PSF (colored boxes). Right top: Raw pixel voltage integration ramps of the pixels selected in the left image (solid colored lines). The dashed colored lines are linear regressions on the first 5 frames of the selected ramps. The blue ramp has been shifted down by 2000 DN for clarity. Right bottom: Subsequent frame differences of ramps shown in the top right panel ($\Delta DN = DN_{i+1} - DN_i$). The dashed colored lines are the slopes determined from the linear regressions on the first 5 frames of the selected ramps.

The non-linearity is wavelength-dependent due to the absorption coefficient of the Si:As infrared-active layer being wavelength-dependent. Up to 15 μm the absorption coefficient is well described by Eq. 3 (Woods et al. 2011; Rieke et al. 2015).

$$\alpha(\lambda) = 102 * (\lambda/7\mu m)^2\ cm^{-1} \quad (3)$$

The quadratic dependence in Eq. 3 implies that longer-wavelength photons have a higher probability of being absorbed closer to the buried contact. That in combination with the decrease in the width of the depletion region (Eq. 2) means that the reduction in response will be greater at longer wavelengths.

2.4. The issue with defining a global MIRI non-linearity solution for all illumination profiles

For the MIRI Imager, for a single wavelength filter, the *JWST* MIRI data calibration pipeline uses a non-linearity solution that is common for all the pixels on the detector. Assuming a perfectly uniform detector illumination and a perfectly uniform response for all pixels, this would imply a single global correction, derived as per the process described in Sect. 2.3 and illustrated in Fig. 2. In this simple case the uncertainties on the non-linearity solution would be linked to read-out noise, photon-noise, dark current noise, and the reset effects impacting the start of MIRI ramps (Morrison, et al. 2023). Although one would expect the global "classical" non-linearity solution to hold for all types of illumination – and indeed it does for low-contrast extended and semi-extended sources – it fails in regions of high contrast, for example for point sources. This is notably of concern at the shorter MIRI wavelengths (5-15 μm) because at longer wavelengths (above 15 μm) the JWST thermal background increasingly reduces the signal contrast between the science target and the surrounding background.

In Fig. 5, in the left panel, we show a small section of the MIRI Imager field of view where a bright unresolved (point) source was observed in flight during a multi-instrument multi-field *JWST* in-focus test[2]. Here, the MIRI Imager F560W bandpass filter was used and the telescope Point Spread Function (PSF) in the F560W filter can be discerned. We select six pixels that cross the core of the PSF in the horizontal direction, and plot the raw pixel voltage integration ramps in the top right panel of Fig. 5 (solid colored curves). We note that the green-colored ramp is the same as the ramp we showed in Fig. 2, where here we show the full extent of the ramp going well past saturation. The green and the red-colored ramps record a similar output level and display a non-linear behavior that is well understood in the context of a uniform detector illumination. However, we see that the ramp of the orange-colored pixel, located one square to the left of the green pixel on the detector, shows a signature that deviates strongly from the classical understanding of the MIRI ramp non-linearity. Instead of a decrease in slope, the slope increases.

Clearly, the solution that linearizes the green-colored ramp cannot linearize the orange-colored ramp. Quite the contrary, correcting the orange-colored ramp with the same solution as

[2] `https://www.stsci.edu/jwst/science-execution/program-information.html?id=1464`

the green ramp will result in the former curving even more upwards. This is important because the *JWST* calibration pipeline determines the flux of a source by performing a linear regression on the non-linearity corrected ramps.

In the right bottom panel of Fig. 5 we show the subsequent frame differences of the ramps of the selected pixels. The solid curves show the impact of the reduction of the depleted region width on the determined slopes. The dashed lines illustrate the estimated slopes based on the output level in the first five frames of the raw ramps (top right panel). For the orange and the purple-colored ramps the ΔDN values are anomalous until the green and red-colored ramps saturate. Then the orange and the purple-colored ramps appear to follow a "classical" non-linearity. As the purple-colored ramp reaches saturation, the olive-colored ramp starts to deviate upwards. This link is less prominent for the orange and blue ramps, though a hint of the same effect can be discerned for the blue ramp at this highest frame numbers.

3. Observations and MIRI BFE impact on science

3.1. The impact of the MIRI BFE on the Imager PSF

The data reduction workflow for *JWST* data involves performing a linear regression on each of the pixel voltage integration ramps after these have been corrected for electronic effects; this includes the non-linearity correction (Morrison, et al. 2023). If the impact of the MIRI BFE, as seen in Fig. 5, is not corrected or mitigated, the final estimated slope values from the linear regression (measured in DN per second) end up being systematically higher. The impact of this on the MIRI Imager PSF is shown in Fig. 6. We compare the case where, after applying the *JWST* MIRI non-linearity correction, the slope values are computed from performing a linear regression on all the non-saturated frames in each ramp, versus only the first 20 frames in each ramp. We then fit a 1D Voigt profile[3] to the sampled Imager PSF and estimate the profile Full-Width at Half-Maximum (FWHM) empirically based on where the fitted profiles have a signal value equal to half of the peak. The FWHM values of the two Voigt profile fits differ by 25% and the integral of the Voigt profile in the case of the full ramp fit (orange profile) is 8.5 % larger than the 20 frame ramp fit. Conclusively, when using all the non-saturated frames in the ramps, the resulting PSF is fatter and the source integrated photometry makes it appear brighter.

To mitigate the impact of the MIRI BFE, the *JWST* pipeline flags the pixels that reach the saturation limit and then flags the frames of all surrounding pixels past the frame where the bright pixels saturate. These flagged frames are then not used in the slope determination of the surrounding pixels. In the case of Fig. 5, the ramp of pixel X=572 saturates first at group number 56, hence for the ramps of pixels X=571 and X=573 only the part of the ramp up to frame number 56 is used to fit the slope. Performing the same exercise as for Fig. 6, even with this mitigation strategy, the MIRI BFE still broadens the PSF by a factor of ~10 % and the integrated photometry varies by ~0.5 %.

There are two straight-forward ways that the MIRI BFE impacts the scientific interpretation of the MIRI Imager data. Firstly, when it comes to astronomical imaging of point sources, astronomers perform aperture photometry by estimating the sum of the flux inside a circle with a radius that contains the largest fraction of the flux and minimizes the contribution of the background to said flux. Limiting this radius to the PSF core, aperture correction factors are applied to account for the fraction of the PSF present outside the aperture that is not accounted for. Given that the MIRI BFE broadens the PSF, this results in a systematic effect on the absolute flux calibration depending on the brightness of the source. A simple mitigation is to use aperture photometry with a relatively large aperture; it is probably also feasible to derive signal-dependent aperture corrections to transfer from a bright source with a large aperture to faint ones measured with smaller apertures. Secondly, a different method to extract integrated fluxes from a point source is by performing PSF-weighted photometry. For this, an accurate model of the PSF is required, so that the weights used for each pixel are representative of the detector illumination. Such a model PSF can be derived empirically, however, bright sources are preferred for this. Applying a model PSF based on bright source measurements, that are impacted by the MIRI BFE, on faint sources where the PSF-weighted photometry provides the biggest advantage, will result in the technique not meeting the theoretical noise-reduction predictions.

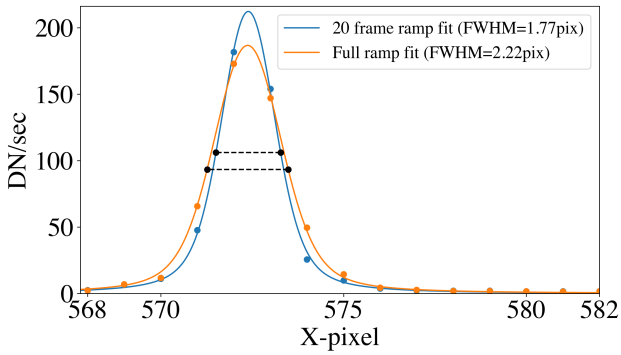

Fig. 6. MIRI Imager PSF based on pixel ramp slope fits (20 frames versus full ramp). 1D Voigt profiles are fitted to the two PSFs and the FWHM is estimated based on where the fitted profiles have a signal value equal to half of the peak. The MIRI BFE results in a percentage change between the widths of the PSF of 25% in the case where the full ramp is used for the slope fitting.

3.2. The impact of the MIRI BFE on the Low Resolution Spectrometer PSF

The MIRI Low Resolution Spectrometer (LRS) data are imaged on a subarray of the MIRI Imager detector. During the *JWST* Cycle 1 calibration phase a series of flux calibration activities was performed by observing flux calibration standards[4]. In the left panel of Fig. 7 we show the LRS spectrum of a time-series observation of BD+60 1753 observed with the LRS slitless prism.

To study the impact of the MIRI BFE on the LRS PSF we use the recorded signal in a row of detector pixels that cross a bright part of the spectrum. In the top right panel of Fig. 7 we show with solid lines four raw voltage integration ramps belonging to four of the pixels that sample the LRS PSF. We notice that none of the ramps reach saturation; this means that the BFE mitigation strategy currently implemented in the *JWST* pipeline is not applicable here. The non-linearity corrected ramps are plotted as loosely dotted lines. The assumption is that, since these ramps have been non-linearity corrected, subsequent frame differences should yield the same mean slope. In the middle right panel of Fig. 7 we plot the LRS sampled PSF by taking two

[3] The fitting was performed using the `astropy.modeling` python package (Astropy Collaboration et al. 2013, 2018).

[4] `https://www.stsci.edu/jwst/science-execution/program-information.html?id=1536`

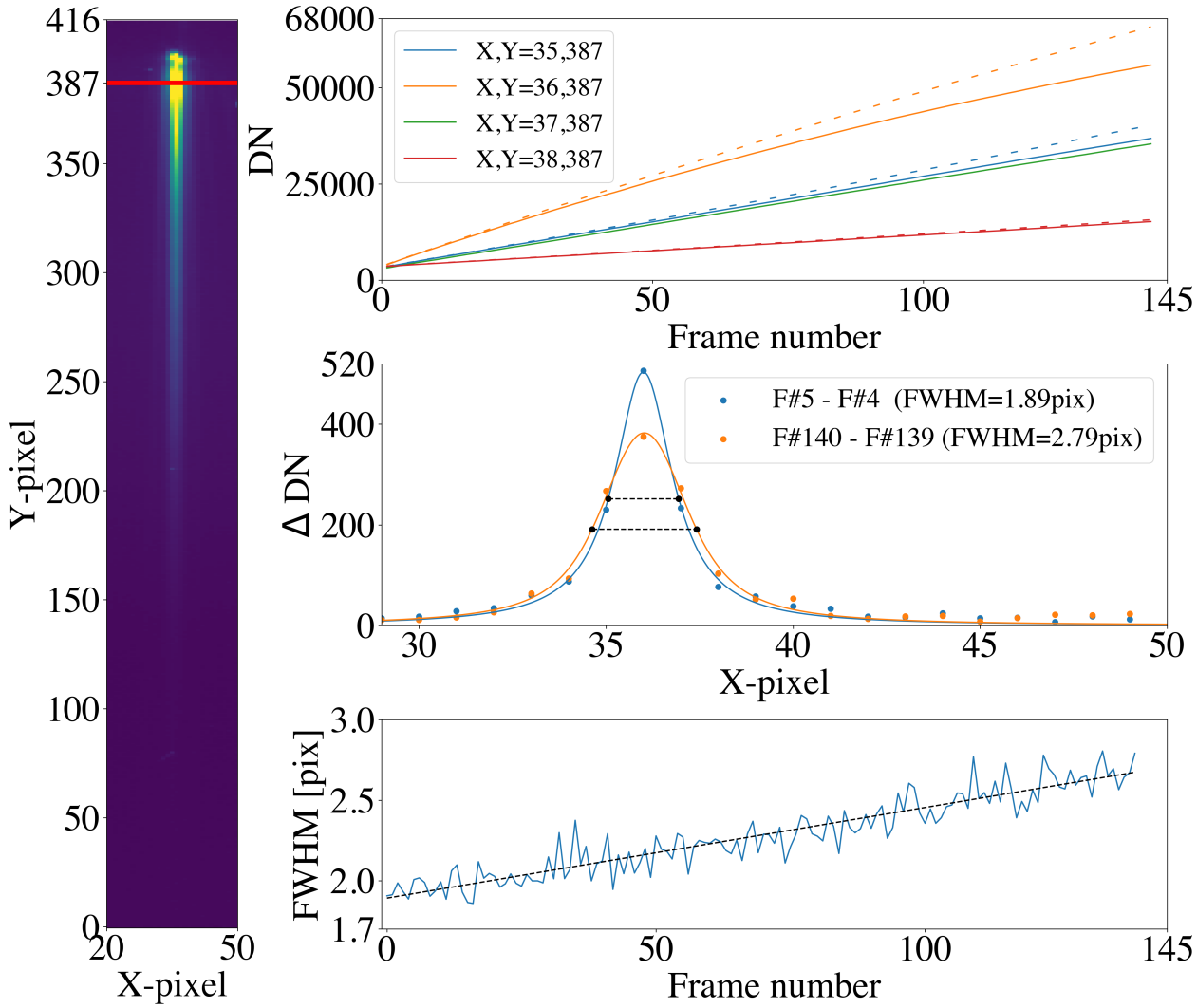

Fig. 7. Left: Detector-level reduced MIRI LRS data of a point source. One pixel row is selected to examine how the MIRI BFE impacts the LRS PSF (red horizontal line). Right top: The solid lines are the raw pixel voltage integration ramps of the pixels sampling the PSF. The loosely dashed lines are the non-linearity corrected ramps. Right center: Sampled PSF estimated from two sets of frame differences. 1D Voigt fits to the sampled PSFs are overplotted. Right bottom: LRS PSF FWHM estimated by taking subsequent frame differences along the length of the linearized ramps and fitting 1D Voigt profiles.

sets of frame differences, one set at the start of the non-linearity corrected ramp, and one set at the end of the ramp. 1D Voigt profiles are fitted to the two sampled PSFs. The FWHMs of the fitted Voigt profiles are significantly larger at the end of the ramp compared to the beginning of the ramp. This is quantified further in the lower right panel where the fitted PSF FWHM is seen to grow linearly along the ramp. This result implies that the ramps are not linearized; they show an increase in slope in the PSF wings and a decrease in slope in the PSF core. This is in line with the result shown in Fig. 6.

In reality, each pixel on the left panel of Fig. 7 recorded 212 integration ramps as part of the time-series observation of BD+60 1753 to characterize the photometric stability of the instrument. One of the major science cases for the LRS is observing exoplanet transits (Bouwman et al. 2022). These transits can sometimes result in up to a few percent change in the brightness of the host star depending on the relative star-to-planet size (for example in the LRS data of HD189733b). Conceptually, this implies that for the integration ramps in transit, the ramps will reach a lower DN value compared to the integration ramps that are out of transit. Based on the bottom right panel of Fig. 7, this will then result in a different PSF FWHM. Although the magnitude of the effect will be small (FWHM systematic of 5% of a pixel for the LRS data of HD189733b), exoplanet signals are also buried into noise, hence the relative effect can be significant.

3.3. *The impact of the MIRI BFE on Medium Resolution Spectrometer data of spectrally unresolved emission lines*

In the case of MIRI observations of spectrally unresolved emission lines taken with the Medium Resolution Spectrometer (MRS), the line spread function (LSF) will be broadened in a similar fashion to the PSF shown in Fig. 6. To illustrate this science case, in Fig. 8 we show the impact of the MIRI BFE on an unresolved emission line of the Cat's Eye Nebula NGC 6543 which was observed during the JWST commissioning phase[5]. The top left panel shows half of the MRS SW detector (columns

[5] https://www.stsci.edu/jwst/science-execution/program-information.html?id=1031

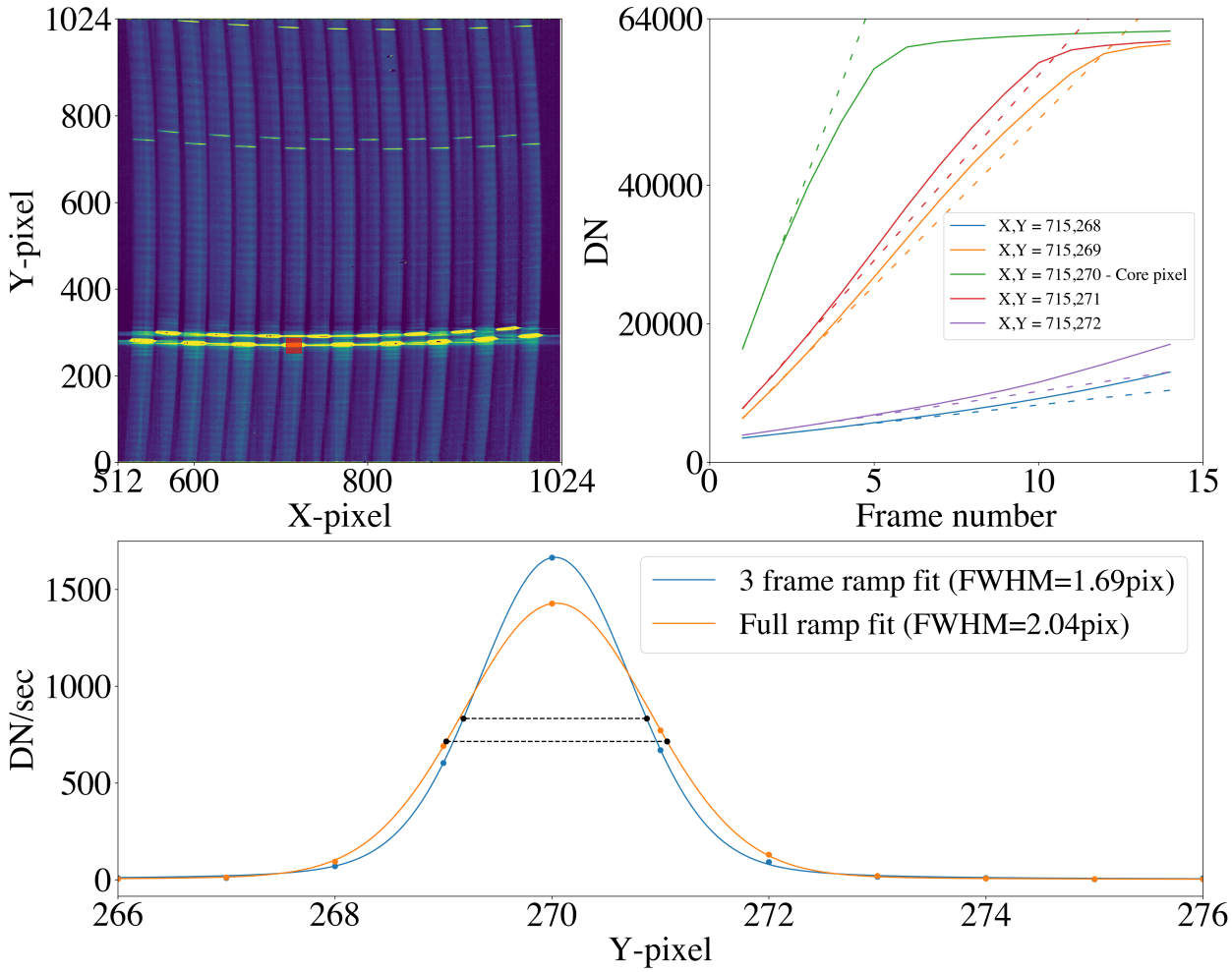

Fig. 8. Top left: Detector-level reduced MIRI MRS data of the spatially extended Cat's Eye Nebula (NGC 6543) in the 9.94–11.87 μm range. A small region of interest (red box) is selected on a bright emission line. Top right: Raw pixel voltage integration ramps of the pixels selected in the left image (solid colored lines). The dashed colored lines are produced from linear fits to the first 2 frames in each ramp. Bottom: 1D Voigt fitted profile to the estimated emission line flux.

512 to 1024) covering the 9.94–11.87 μm range. A number of curved strips can be observed; these correspond to slits positioned on the sky of which the light is spectrally dispersed in the detector vertical direction along the strip curvature. Since NGC 6543 is spatially resolved, all strips on the detector show flux from the spatially extended emission. We choose five pixels in the vertical direction covering the brightest emission line (location of red dot in the plotted panel). In the top right panel we show the shapes of the raw ramps which all visibly curve up due to the MIRI BFE except for the one sampling the peak of the MRS LSF. The bottom panel of Fig. 8 shows the impact of the BFE on the determined shape of the emission line.

One recurring remark between the Imager, LRS, and MRS data is that the signal in the core of the PSF, where the behavior of the non-linearity qualitatively follows the classical trend, also decreases at higher DN levels. This suggests that the non-linearity correction, derived from an extended illumination, does not perfectly linearize the ramps that sample the core of the PSF either.

3.4. MRS spectral fringing and deriving an MRS non-linearity solution in the presence of BFE

The MIRI MRS suffers from significant spectral fringing caused by Fabry-Pérot interference inside the MRS detectors (Argyriou et al. 2020a,b). The fringing modulates the spectral baseline by up to 30% of the continuum with a period between 12 and 30 pixels. For point sources the fringe properties depend on (i) the profile of the MIRI pupil illumination, (ii) the part of the wavefront phase map that is sampled by the detector pixels, (iii) the wavelength of the in-falling light, (iv) the local geometry of the detector and (v) the refractive properties of the detector-constituting layers. For spatially extended sources the fringes depend only on (iii, iv, v). Nevertheless, this contrast of up to 30% on the continuum results in a BFE-induced uncertainty on the derived non-linearity solutions. Contrary to the MIRI Imager where a uniform illumination can be achieved, and the large band-pass blurs the fringes, for the MRS disentangling the MIRI BFE from the ramp non-linearity has not been achievable.

The uncertainty on the global MRS non-linearity solution per spectral band is minimized by using the ramps of the pixels that sample the fringe peaks across the detector (Morrison, et al. 2023). However, there is still a significant spread in the non-linearity solutions derived from the different pixels, and that

is because (1) the MRS spectra are curved on the detector, as shown in the top left panel of Fig. 8 and (2) the BFE is likely represented by a 2D kernel. As such, fringe peaks can interact differently with their surrounding neighbors.

3.5. Implications of BFE on high contrast (coronographic) imaging

A well characterized PSF is critical for high contrast imaging. As an example, Gaspar et al. (2023, Nature Ast. In press) found that exquisitely good PSF subtraction could be achieved at 25.5 μm using a reference star (19 PsA) of very similar brightness to the science target (Fomalhaut). Attempts to build and use a synthetic PSF using WebbPSF were far less successful. Until now the cause of the unsatisfactory performance of the synthetic images was attributed predominantly to the effect of detector scattering, which causes a cruciform in the Imager and LRS PSF, and significant PSF broadening and excess power in the wings for the MRS PSF up to 12 μm (Gáspár et al. 2021; Kendrew, et al. 2023; Argyriou, et al. 2023). The BFE is introducing an additional systematic on the PSF and LSF, one that is dependent on the covered dynamic range of the pixels. Patapis et al. (2022) used MIRISim (Klaassen et al. 2021), an instrument simulator with imaging based on WebbPSF, to evaluate the ability to obtain high quality MRS spectra of exoplanets. An understanding of the BFE is desirable to enhance the accuracy of such spectra and to allow obtaining them relatively close to the host stars. The ultimate performance of MIRI coronagraphy depends on utilization of a PSF reference star (Boccaletti et al. 2022). Again, matching the star to the science target brightness is likely to improve the quality of this procedure. These issues can be mitigated by appropriate planning of observations, particularly given that the telescope shows high stability and wavefront drifts are small, even after large slews, providing a large selection of possible reference stars. Given that coronagraphic and high contrast imaging will use a limited number of spectral bands, additional flexibility may be possible by building empirical models of the image as a function of brightness.

4. Modeling

4.1. Setting up the MIRI Si:As IBC detector array electrostatic model using `Poisson_CCD`

The public code `Poisson_CCD`[6] solves Poisson's electrostatic differential equation given by Eq. 4 numerically, in 3 spatial dimensions, and simulates charge transport within CCDs (Lage et al. 2021). The potentials and free carrier densities within a CCD are self-consistently solved for, giving realistic results for the depletion profile and electron paths followed in silicon.

$$\nabla^2\phi(x,y,z) = \frac{\rho(x,y,z)}{\epsilon_{Si}}, \tag{4}$$

where ϕ is the electrostatic potential, ρ is the charge density, and ϵ_{Si} is the dielectric constant of silicon.

Contrary to CCDs where the entire silicon substrate needs to be accounted for, in the case of the Si:As IBC detectors only the narrower infrared-active layer needs to be modelled. For this, an input file is defined with all necessary parameters to solve Eq. 4 numerically. The MIRI-specific parameters are tabulated in Table 1, where some of these parameters were previously mentioned in Sect. 2.3 and 2.2.

The doping level of the contacts `ContactDose_0` of N=7.5 $*$ 10^{18} cm^{-3} was estimated in Argyriou et al. (2020a) by modelling the high and low frequency fringing present in MRS data[7]. The parameter `Lambda` is used in conjunction with Eq. 3, implemented into the `Poisson_CCD` code, to estimate a probability for a photo-excited electron to be produced in the infrared-active layer.

One of the simplest simulation setups in `Poisson_CCD` is shown in Fig. 9 for MIRI. Here a 5-by-5 pixel grid is used, as seen in the top left panel staring down at the detector pixels. The front contact voltage is set at the value of `V_contact` and the buried contact voltage is set by `V_bb` defined in Table 1. A localized debiasing `DeltaV_0_0`=-1.5 V is applied at the center pixel. The variation of the electrostatic potential $\phi(x,y,z)$ across the depth of the infrared-active layer is shown in the top right panel. Finally the concentration of holes in the infrared-active layer is shown in the bottom panel. The blue shading illustrates where the active layer is depleted, while the yellow and red shading denotes areas where the layer is undepleted. The top 1 μm (dark red shading) is the location of the buried contact. The 1 μm-thick dark red shading at Z=0 μm is the location not covered by the front contact which itself rests on the pixel metallization, illustrated in Fig. 1.

4.2. Electrostatic simulation for imaging case

To perform a realistic MIRI simulation of a point source illumination on the detector, the `Poisson_CCD` code is run with a random set of tracers (photons) pooled from a 2D Gaussian pattern. The Gaussian pattern widths in x and y-directions are defined in Table 1 based on a 2D Gaussian fit to the 20 frame ramp fit in Fig. 6 (σ_x=σ_y=0.56 pix, equivalent to `Sigmax` = `Sigmay` = 14 μm). `Poisson_CCD` first solves Eq. 4, then a distinct number of tracers are injected into the model. Every time a tracer results in a photo-excited electron (produced at a given pixel based on the absorption length of Eq. 3), the path of the photoelectron, dictated by the electric field inside the layer, is numerically computed and the pixel at which the photoelectron ends up is recorded. The photoelectric charge accumulation introduces a debiasing at each pixel as defined by the `ContactCapacitance` parameter. The updated debiasing level at each pixel is used to solve Eq. 4 again in the next step. Performing such a simulation self-consistently results in each pixel shown in the top left panel of Fig. 9 experiencing a different level of debiasing. Pixels that see more tracer photons will have more photoelectrons generated above them, increasing the resulting debiasing, and reducing the width of the depletion region as a result. The impact of the debiasing on the path of the electrons is monitored by tracking the electron paths in the active layer.

In Fig. 10, we show five simulation run steps where 1, 15, 40, 55, and 85 times N=20,000 tracers were injected into the model, distributed over a 2D Gaussian profile. In the left column of plots the level of debiasing at each pixel is shown. In the middle column we show where each produced photoelectron lands on the geometric grid. In the right column the photoelectron paths are tracked from their creation site down to the pixels (the code does this in both x- and y-directions but we only plot the paths in the

[6] `https://github.com/craiglagegit/Poisson_CCD/tree/master`

[7] In case a smooth Gaussian profile is preferable for the doping distribution across the contacts the `Poisson_CCD` parameters `ContactDose_0`, `ContactPeak_0`, and `ContactSigma_0` can be used to produce the required integrated doping level.

Table 1. MIRI Si:As IBC detector electrostatic model parameters inputted to `Poisson_CCD`.

Parameter	Value [unit]	Description
`V_bb`	-4.0 V	Back bias voltage at buried contact (Ressler et al. 2015)
`V_contact`	-2.0 V	Contact voltage at front contact
`ContactCapacitance`	33.6 fF	Capacitance at amplifier integrating node
`RecombinationLifetime`	$2 * 10^{-7}$ sec	Electron recombination time (Rieke et al. 2015)
`TopDopingThickness`	1.0 μm	Thickness of buried contact
`TopSurfaceDoping`	$-7.5 * 10^{18}$ cm^{-2}	Doping buried contact (Argyriou et al. 2020a)
`BackgroundDoping`	$-1.5 * 10^{12}$ cm^{-2}	Density of minority impurity concentration in infrared-active layer
`BottomOxide`	1.0 μm	Bottom oxide thickness above pixel metallization
`ContactDose_0`	$7.5 * 10^{18}$ cm^{-2}	Doping of front contact
`ContactWidth`	20.0 μm	Width of front contact
`ContactHeight`	20.0 μm	Height (not thickness) of front contact
`SensorThickness`	35 μm	Infrared-active layer thickness
`PixelSizeX`	25 μm	Pixel size in x (Rieke et al. 2015)
`PixelSizeY`	25 μm	Pixel size in y
`Sigmax`	14 μm	Sigma of light profile (based on 20 frame ramp Gaussian fit in Fig. 6)
`Sigmay`	14 μm	Sigma of light profile (set equal to `Sigmax`)
`CCDTemperature`	6.4 K	Operational temperature of MIRI detectors
`Lambda`	5.6 μm	Wavelength of incoming light

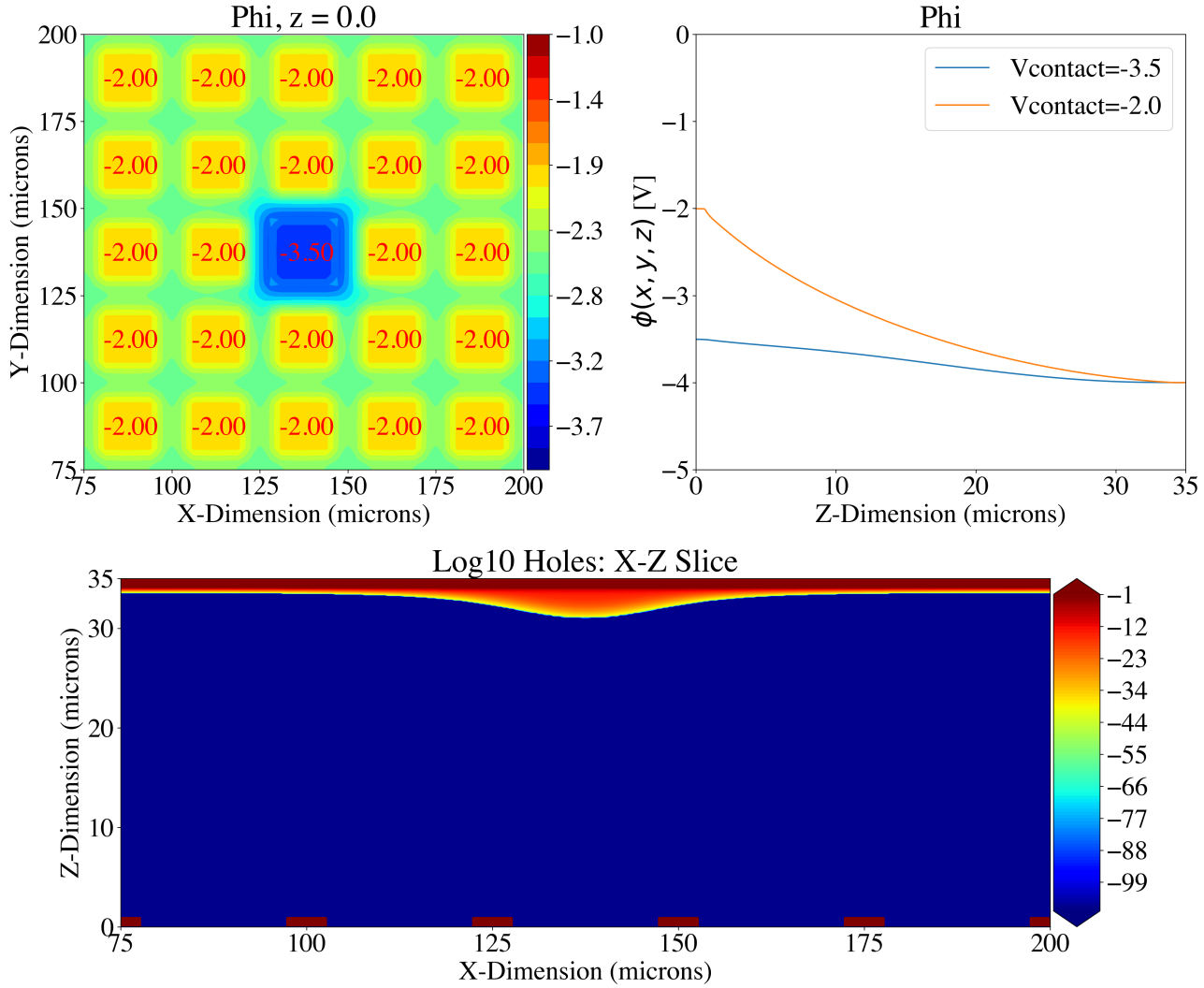

Fig. 9. `Poisson_CCD` output plot of basic MIRI detector model simulation. Top left: Poisson's equation is solved for a 5-by-5 grid of pixels where a localized voltage debias of -1.5 V is applied at the middle pixel. Top right: The electrostatic potential is shown as a function of detector depth. Z=0 μm is located at the pixel, Z=35 μm is located at the top of the buried contact. Bottom: The MIRI detector infrared-active layer. The blue shading shows areas where the active layer is fully depleted. Yellow and red shading show areas where the active layer is undepleted. The buried contact is located at Z=34–35 μm. The dark red boxes at Z=0–1 μm illustrate the regions not covered by the detector front contact.

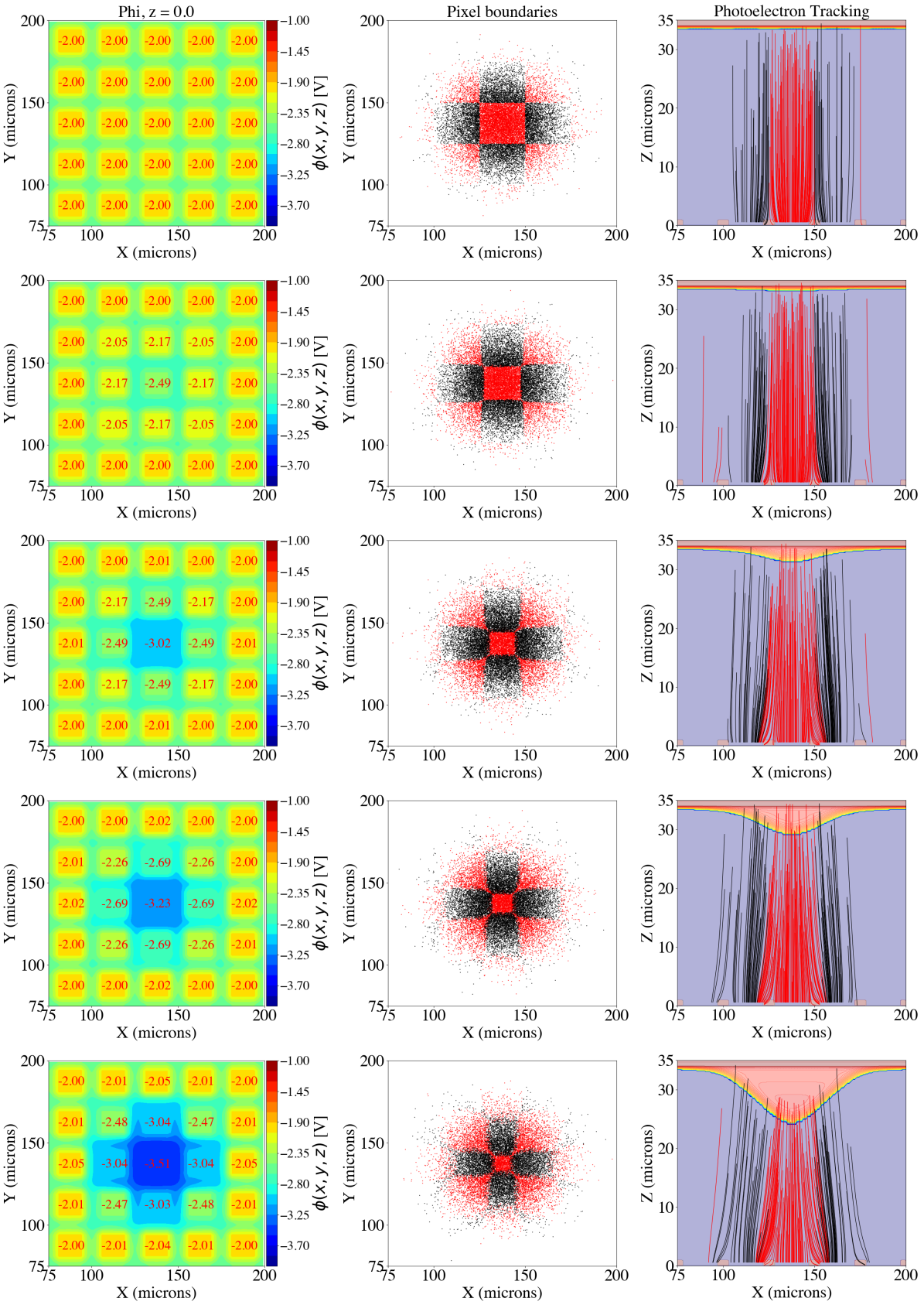

Fig. 10. Brighter-Fatter Effect in MIRI detector model simulation. Left column: Distribution of the electrostatic potential ϕ across the 5-by-5 simulation pixel grid. Middle column: Location on the pixel geometric grid where each produced photoelectron landed. Neighboring pixels are given alternating colors. This probes the effective pixel collecting area change due to the debiasing. Right column: Photoelectron generation in infrared-active layer and photoelectron path tracking. Going from the top to the bottom row, the model is injected with 1, 15, 40, 55, and 85 times N=20,000 tracers.

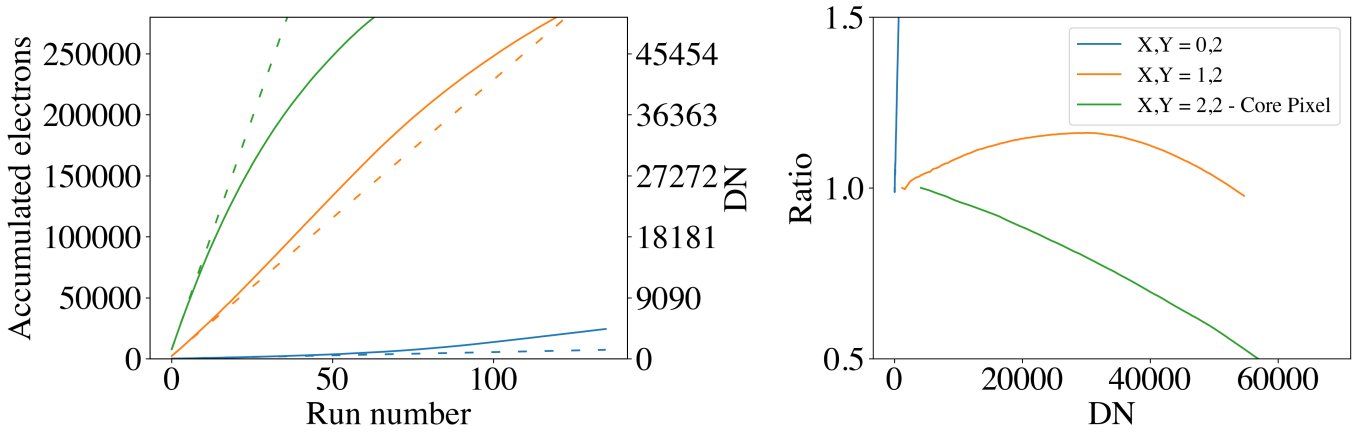

Fig. 11. Left: Charge accumulation in three of the simulated pixels of Fig. 10. The dashed lines are linear regressions to the first three samples in each ramp. The number of electrons can be converted to DN using the pixel gain of 5.5 e-/DN (Rieke et al. 2015). Right: Ratio of charge accumulation ramps and their respective linear fits. The ratio illustrates the non-linear behavior of the ramps in the presence of the MIRI BFE.

detector x-direction). The paths are overplotted on the concentration of holes in the infrared-active layer, which probes the areas of depletion and undepletion in the layer. The rows of plots go from lower debiasing in the top row to higher debiasing in the bottom row.

Due to the larger accumulation of photoelectrons in the central pixel, it records a larger debiasing level compared to its neighboring pixels. The `Poisson_CCD` code is able to self-consistently update the debiasing across the 5-by-5 pixel grid. In the middle column of Fig. 10 a decrease in the area of the (red) central pixel can be noticed from the top to the bottom row. This reduction in effective photocollecting area is explained by the plots in the right column. The panel in the bottom row shows clearly that photoelectrons produced above the central pixel are guided by the electric field to the neighboring pixels instead. In addition, in the same panel it can be noticed that a significant portion of the infrared-active layer is undepleted, and photoelectrons produced in that area recombine after a time span of `RecombinationLifetime` and are effectively "lost", i.e. they are not detected. Figure 11 shows the number of accumulated electrons in three of the simulated pixels (the results are symmetric due to the centered simulated PSF). This is the output that is most directly applicable and comparable to the MIRI detector voltage integration ramps shown in the top right panel of Fig. 5. In the right panel we can see that there is a transition in the non-linearity solution from the core pixel (2,2) to the outer pixel (0,2) due to the migration of electrons from the core pixel to the neighboring pixels. Applying the non-linear response of the core pixel to the neighboring pixels results in an overestimation of the number of accumulated electrons.

5. Discussion

The results shown in Fig. 10 and 11 converge to four important outcomes: (1) They provide strong evidence for the physical mechanism causing the MIRI BFE for point sources (and any source with a flux contrast on the detector). The MIRI BFE is caused by the detector debiasing altering the configuration of the 3D electrostatic potential $\phi(x, y, z)$ inside the Si:As IBC sensor infrared-active layer. The corresponding electric field then guides photo-excited electrons away from the pixel above which they were generated into neighboring pixels. Linking this back to the ramp plots shown in the right panel of Fig. 5 and the top right panel of Fig. 8, at higher DN levels the debiasing in the central pixel results in an increasing fraction of photoelectrons being detected at the neighboring pixels instead, causing an increase in the measured ramp slopes of the neighboring pixels. Furthermore, this effect can extend to the pixels not directly neighboring the central pixel, as those that do neighbor the central pixel also start contributing to their own neighbors as seen in the bottom two panels of the right column in Fig. 10 and the right panel of Fig. 11. (2) The increasing size of the active layer undepleted region increases the number of photoelectrons lost via recombination. This is the physical mechanism driving the MIRI non-linearity. Interestingly, even though at higher debiasing levels the photoelectrons that are detected start their path closer to the pixels, these are still guided to the neighboring pixels by the electric field. (3) The profile of the undepletion region contour is approximately flat in the center pixel and shows a significant gradient over the span of a pixel width in the neighboring pixels. This implies that (a) the center pixel will have a non-linearity solution most akin to that of a spatially uniform (extended) source, however, (b) the photoelectron collection profile likely has an intra-pixel dependence on where the centroid of the source is. (4) Based on the previous three points, it is clear that the MIRI detector non-linearity and BFE cannot be considered to be independent of one another in terms of calibrating the two effects.

We have provided supporting evidence that the physical mechanism of the Si:As IBC detector BFE is fundamentally different from the type of BFE that CCDs and H2RG detectors suffer from. In the latter case an electric field at the pixel is created due to the accumulation of photoelectrons at the pixel potential well. This electric field increases in strength and, via the mechanism of electric repulsion, forces incoming photoelectrons to move to the neighboring pixels. Although the resulting impact manifests the same way in the Si:As IBC detector and CCD and H2RG case, the distinction is important given that BFE was not considered possible for MIRI since the photoelectrons are not stored at the pixels, hence they cannot cause the CCD and H2RG type of BFE. As such we term the effect described in this paper as "debiasing-induced Brighter-Fatter Effect".

The `Poisson_CCD` model presented in this paper could in theory be used to derive a simultaneous correction for the debiasing-induced BFE and non-linearity in MIRI Imager data, however, this falls outside the scope of this paper. In the case of MIRI/MRS spectroscopy, such an endeavor is more complex given that the spectral continuum is dispersed in curved strips on the detector as shown for example in the top left panel of Fig. 8.

Nevertheless, we argue that the presented work can be used as a foundation for understanding the behavior of detectors similar to Si:As IBC detectors arrays to non-uniform illumination patterns, and also inform the conditions under which the detectors should be operated.

One promising empirical correction for the non-linearity and debiasing-induced BFE, applicable to point sources, is to observe a reference star and derive a ramp model for each part of the PSF. Since the debiasing effect on the ramps is relative, the brightness of the observed sources is not a parameter in the correction. By using the reference star ramps to calibrate the ramps of the science target, an optimal flux calibration can be achieved. This is already being used to improve the phase curve of HD189733b with the LRS. Given the pointing stability of JWST, such a correction would yield positive results for all observing modes of MIRI. This analysis will be expanded upon in a follow-up paper.

6. Conclusions

A debiasing-induced BFE makes the *JWST* MIRI data yield a 10 – 25 % larger and 0.5 – 8% brighter PSF and LSF as a function of the output level dynamic range covered by the detector pixels during an integration. This affects aperture-corrected photometry, PSF-weighted photometry, PSF subtraction, high-contrast imaging, as well as estimates of kinematics based on spectral line profiles. It also directly affects the calibration of MIRI raw ramp data, translating into a systematic uncertainty on the absolute flux calibration as a function of the exposure parameters used to observe flux calibration standards.

Using the public `Poisson_CCD` code and a simple model for the MIRI Si:As IBC sensor infrared-active layer, we found strong evidence for the physical mechanism of the BFE impacting the MIRI pixel voltage integration ramps. We find that this mechanism is driven by detector debiasing due to photoelectron accumulation. This debiasing changes the electrostatic potential inside the infrared-active layer. The paths followed by the excited photoelectrons to the pixels are dictated by the corresponding electric field. At higher levels of debiasing the photoelectrons generated above a given pixel are guided to the neighboring pixels instead. This results in an increase in the slope of the pixel integration ramps as opposed to the decrease in slope recorded for spatially uniform sources.

While the electrostatic potential results in the electrons being guided to neighboring pixels, the debiasing also results in the infrared-active layer becoming more undepleted. This means that more electrons are lost due to recombination, and this constitutes the classical MIRI non-linearity effect. We argue that for point sources, and for sources with a significant spectral and spectral flux contrast, the non-linearity and the BFE cannot be considered to be independent. An accurate pixel integration ramp model needs to account for both. Only applying a non-linearity solution derived based on an extended source illumination to non-uniform illumination will result in systematically larger uncertainties in flux calibration.

Having presented a numerical model that predicts the performance of the MIRI Si:As IBC detectors under non-uniform illumination, this forms a basis to understand the ground test and flight MIRI data. MIRI data in flight can be used to refine the presented model, however, the power of the model lies in better interpreting the MIRI flux systematics, deriving an empirical correction based on ramps of reference stars, and informing the detector operation of future infrared missions.

Acknowledgements. Ioannis Argyriou and Danny Gasman thank the European Space Agency (ESA) and the Belgian Federal Science Policy Office (BELSPO) for their support in the framework of the PRODEX Programme. Ioannis Argyriou would also like to personally thank Eddie Bergeron (STScI) for his investigations of the Brighter-Fatter Effect across the multiple *JWST* instruments and detectors. Craig Lage gratefully acknowledges financial support from DOE grant DE-SC0009999 and NSF/AURA/LSST grant N56981CC.
J. A-M acknowledges support by grant PIB2021-127718NB-100 by the Spanish Ministry of Science and Innovation/State Agency of Research MCIN/AEI/10.13039/501100011033 and by "ERDF A way of making Europe". Alvaro Labiano acknowledges the support from Comunidad de Madrid through the Atracción de Talento Investigador Grant 2017-T1/TIC-5213, and PID2019-106280GB-I00 (MCIU/AEI/FEDER,UE).
The work presented is the effort of the entire MIRI team and the enthusiasm within the MIRI partnership is a significant factor in its success. MIRI draws on the scientific and technical expertise of the following organisations: Ames Research Center, USA; Airbus Defence and Space, UK; CEA-Irfu, Saclay, France; Centre Spatial de Liége, Belgium; Consejo Superior de Investigaciones Científicas, Spain; Carl Zeiss Optronics, Germany; Chalmers University of Technology, Sweden; Danish Space Research Institute, Denmark; Dublin Institute for Advanced Studies, Ireland; European Space Agency, Netherlands; ETCA, Belgium; ETH Zurich, Switzerland; Goddard Space Flight Center, USA; Institute d'Astrophysique Spatiale, France; Instituto Nacional de Técnica Aeroespacial, Spain; Institute for Astronomy, Edinburgh, UK; Jet Propulsion Laboratory, USA; Laboratoire d'Astrophysique de Marseille (LAM), France; Leiden University, Netherlands; Lockheed Advanced Technology Center (USA); NOVA Opt-IR group at Dwingeloo, Netherlands; Northrop Grumman, USA; Max-Planck Institut für Astronomie (MPIA), Heidelberg, Germany; Laboratoire d'Etudes Spatiales et d'Instrumentation en Astrophysique (LESIA), France; Paul Scherrer Institut, Switzerland; Raytheon Vision Systems, USA; RUAG Aerospace, Switzerland; Rutherford Appleton Laboratory (RAL Space), UK; Space Telescope Science Institute, USA; Toegepast- Natuurwetenschappelijk Onderzoek (TNO-TPD), Netherlands; UK Astronomy Technology Centre, UK; University College London, UK; University of Amsterdam, Netherlands; University of Arizona, USA; University of Bern, Switzerland; University of Cardiff, UK; University of Cologne, Germany; University of Ghent; University of Groningen, Netherlands; University of Leicester, UK; University of Leuven, Belgium; University of Stockholm, Sweden; Utah State University, USA. A portion of this work was carried out at the Jet Propulsion Laboratory, California Institute of Technology, under a contract with the National Aeronautics and Space Administration. We would like to thank the following National and International Funding Agencies for their support of the MIRI development: NASA; ESA; Belgian Science Policy Office; Centre Nationale D'Etudes Spatiales (CNES); Danish National Space Centre; Deutsches Zentrum fur Luft-und Raumfahrt (DLR); Enterprise Ireland; Ministerio De Economiá y Competividad; Netherlands Research School for Astronomy (NOVA); Netherlands Organisation for Scientific Research (NWO); Science and Technology Facilities Council; Swiss Space Office; Swedish National Space Board; UK Space Agency. We take this opportunity to thank the ESA *JWST* Project team and the NASA Goddard ISIM team for their capable technical support in the development of MIRI, its delivery and successful integration.

References

Argyriou, I., Rieke, G. H., Ressler, M. E., Gáspár, A., & Vandenbussche, B. 2020a, in Society of Photo-Optical Instrumentation Engineers (SPIE) Conference Series, Vol. 11454, Society of Photo-Optical Instrumentation Engineers (SPIE) Conference Series, 114541P
Argyriou, I., Wells, M., Glasse, A., et al. 2020b, A&A, 641, A150
Argyriou, et al. 2023, JWST MIRI flight performance: The Medium-Resolution Spectrometer, in prep.
Astropy Collaboration, Price-Whelan, A. M., Sipőcz, B. M., et al. 2018, AJ, 156, 123
Astropy Collaboration, Robitaille, T. P., Tollerud, E. J., et al. 2013, A&A, 558, A33
Boccaletti, A., Cossou, C., Baudoz, P., et al. 2022, arXiv e-prints, arXiv:2207.11080
Boccaletti, A., Lagage, P.-O., Baudoz, P., et al. 2015, Publications of the Astronomical Society of the Pacific, 127, 633
Bouchet, P., García-Marín, M., Lagage, P.-O., et al. 2015, Publications of the Astronomical Society of the Pacific, 127, 612
Bouwman, J., Kendrew, S., Greene, T. P., et al. 2022, arXiv e-prints, arXiv:2211.16123
Coulton, W. R., Armstrong, R., Smith, K. M., Lupton, R. H., & Spergel, D. N. 2018, AJ, 155, 258
Dorn, M., McMurtry, C., Pipher, J., et al. 2018, in High Energy, Optical, and Infrared Detectors for Astronomy VIII, ed. A. D. Holland & J. Beletic, Vol. 10709, International Society for Optics and Photonics (SPIE), 52 – 60

Gáspár, A., Rieke, G. H., Guillard, P., et al. 2021, PASP, 133, 014504
Hirata, C. M. & Choi, A. 2020, PASP, 132, 014501
Kendrew, S., Scheithauer, S., Bouchet, P., et al. 2015, Publications of the Astronomical Society of the Pacific, 127, 623
Kendrew, et al. 2023, JWST MIRI flight performance: The Low-Resolution Spectrometer, in prep.
Klaassen, P. D., Geers, V. C., Beard, S. M., et al. 2021, MNRAS, 500, 2813
Lage, C., Bradshaw, A., Anthony Tyson, J., & LSST Dark Energy Science Collaboration. 2021, Journal of Applied Physics, 130, 164502
Lage, C., Bradshaw, A., & Tyson, J. A. 2017, Journal of Instrumentation, 12, C03091
Love, P. J., Hoffman, A. W., Lum, N. A., et al. 2005, in Proceedings of the SPIE, Vol. 5902, Focal Plane Arrays for Space Telescopes II, ed. T. J. Grycewicz & C. J. Marshall, 58–66
McMurtry, C. W., Forrest, W. J., & Pipher, J. L. 2005, in Society of Photo-Optical Instrumentation Engineers (SPIE) Conference Series, Vol. 5902, Focal Plane Arrays for Space Telescopes II, ed. T. J. Grycewicz & C. J. Marshall, 45–57
Moore, Andrew C. 2005, Operating, testing and evaluating hybridized silicon P-I-N arrays, Thesis, [Online; accessed 02-Feb-2023]
Morrison, et al. 2023, JWST MIRI flight performance: Detector Effects and Data Reduction Algorithms, in prep.
Patapis, P., Nasedkin, E., Cugno, G., et al. 2022, A&A, 658, A72
Petroff, M. D. & Stapelbroek, M. G. 1986, Blocked impurity band detectors, uS Patent 4,568,960
Pierret, R. & Harutunian, K. 1996, Semiconductor Device Fundamentals (Addison-Wesley)
Plazas, A. A., Shapiro, C., Smith, R., Huff, E., & Rhodes, J. 2018, PASP, 130, 065004
Ressler, M. E., Sukhatme, K. G., Franklin, B. R., et al. 2015, PASP, 127, 675
Rieke, G. H. 2003, Detection of light: from the ultraviolet to the submillimeter (Cambridge University Press)
Rieke, G. H., Ressler, M. E., Morrison, J. E., et al. 2015, Publications of the Astronomical Society of the Pacific, 127, 665
Wells, M., Pel, J.-W., Glasse, A., et al. 2015, Publications of the Astronomical Society of the Pacific, 127, 646–664
Woods, S. I., Kaplan, S. G., Jung, T. M., & Carter, A. C. 2011, Applied Optics, 50, 4824
Wright, G. S., Wright, D., Goodson, G. B., et al. 2015, Publications of the Astronomical Society of the Pacific, 127, 595
Wright, et al. 2023, The Mid-Infrared Instrument for JWST, PASP, submitted